HHS Public Access

Author manuscript

Sci Signal. Author manuscript; available in PMC 2024 June 08.

Published in final edited form as:

Sci Signal. 2024 April 09; 17(831): eadh1922. doi:10.1126/scisignal.adh1922.

Blocking lipid synthesis induces DNA damage in prostate cancer and increases cell death caused by PARP inhibition

Caroline Fidalgo Ribeiro[1,†], **Silvia Rodrigues**[1,†], **Debora Campanella Bastos**[2], **Giuseppe Nicolò Fanelli**[3], **Hubert Pakula**[1], **Marco Foiani**[4], **Giorgia Zadra**[5], **Massimo Loda**[1,*]

[1]Weill Cornell Medical College, New York, New York, US

[2]University of Campinas, Piracicaba, Brazil

[3]University of Pisa, Pisa, Italy

[4]IFOM/University of Milan, Milan, Italy

[5]Institute of Molecular Genetics, National Research Council, Pavia, Italy

Abstract

Androgen deprivation therapy (ADT) is the primary treatment for prostate cancer; however, resistance to ADT invariably develops, leading to castration-resistant prostate cancer (CRPC). Prostate cancer progression is marked by increased de novo synthesis of fatty acids due to overexpression of fatty acid synthase (FASN), making this enzyme a therapeutic target for prostate cancer. Inhibition of FASN results in increased intracellular amounts of ceramides and sphingomyelin, leading to DNA damage through the formation of DNA double strand breaks and cell death. We found that combining a FASN inhibitor with the poly-ADP ribose polymerase (PARP) inhibitor olaparib, which induces cell death by blocking DNA damage repair, resulted in a more pronounced reduction in cell growth than that caused by either drug alone. Human CRPC organoids treated with a combination of PARP and FASN inhibitors were smaller, had decreased cell proliferation, and showed increased apoptosis and necrosis. Together, these data indicate that targeting FASN increases the therapeutic efficacy of PARP inhibitors by impairing DNA damage repair, suggesting that combination therapies should be explored for CRPC.

One-sentence summary:

*Corresponding author. mloda@med.cornell.edu.
†These authors contributed equally to this work

Author contributions

ML, MF, GZ conceived the idea of the study;
CFR, ML designed, coordinated and oversaw the study;
GZ contributed to the experimental design;
CFR, ML wrote the manuscript;
CFR, SR performed all the experiments described;
CFR, SR, DB, ML analyzed the data;
GNF performed multiplex imaging analysis;
DB, HP, MF contributed to the interpretation of data.
All authors reviewed and approved the final text.

Competing interests

No conflict of interest to be reported.

Blocking lipid synthesis induces DNA damage in prostate cancer and increases cell death caused by PARP inhibition.

INTRODUCTION

The dysregulation of lipid metabolism is a common alteration in prostate cancer cells with increased expression of fatty acid synthase (FASN), the enzyme in *de novo* lipogenesis (DNL) (1–3). FASN is the only eukaryotic enzyme capable of producing palmitate, a saturated fatty acid that plays a major role in cell metabolism, as it can be further elongated and desaturated to generate the range of lipids used in membrane synthesis, energy source and protein post-translational modifications (4). The expression of genes involved in lipid metabolism is androgen-regulated, controlled primarily through the sterol response element-binding proteins (SREBPs) (5). As prostate cancer progresses to castration-resistant prostate cancer (CRPC), SREBPs are upregulated, leading to transcriptional activation of lipid synthesis genes (6). This lipogenic phenotype of prostate cancer represents a metabolic vulnerability that can be exploited therapeutically.

Among lipids with important role in the cellular metabolism are the sphingolipids, a group of molecules that includes ceramides,. Ceramides consist of a sphingoid base attached to a fatty acid residue and play a major role in cell membrane structure and signaling (7). During *de novo* ceramide synthesis, ceramide synthase (CERS) enzymes produce dihydroceramide through the addition of fatty acids to sphinganine, which is then reduced to ceramide. The CERS family include 6 members that show specificity to fatty acids depending on their acyl chain length (8). In this study we characterized the interplay between *DNL* and sphingolipid metabolism.

DNA damage can occur as a result of exogenous agents, such as ionizing radiation and alkylating agents, or endogenous sources, such as reactive oxygen species (ROS). When DNA damage occurs, cells trigger a machinery of repair that can involve different pathways, such as DNA Base excision repair (BER), nucleotide excision repair (NER), single strand break repair (SSBR), homologous recombination (HR), non-homologous end joining (NHEJ), and mismatch repair (MMR) (9). These are the six most important DNA repair pathways in mammalian cells, frequently mutated in cancer. Poly(ADP-ribose) polymerase (PARP) inhibition through Olaparib or Rucaparib has been shown as a promising therapeutic approach for BRCA-mutated tumors, such as breast (10), ovarian (11), pancreas (12) and, prostate cancer (13, 14). The mechanism of action of this class of drugs is based on synthetic lethality: when single-strand DNA (ssDNA) breaks induced by PARP inhibitors cannot be repaired, in HR-deficient cells, they will lead to accumulation of DNA damage that eventually culminates in cell death. BRCAness, defined as the suppression of HR, is commonly associated with mutations in *BRCA1* and *BRCA2* genes. The frequency of BRCA alterations in advanced prostate cancer, however, is limited. Only 10% of CRPC patients harbor deleterious *BRCA2* alterations, while the number is even lower for *BRCA1*, at only 2% of patients (15), limiting the patient population that can benefit from this therapy. Nonetheless, other genomic alterations such as the *TMPRSS2:ERG* gene fusion and PTEN deletion have been shown to sensitize cells to PARP inhibition by upregulating double-

strand DNA (dsDNA) break formation (16, 17). Pharmacologically-induced BRCAness represents an alternative to expand the benefit of PARP inhibitors to patients that do not harbor genetic alterations that impair HR. Here, we propose that this can be achieved through the inhibition of DNL.

To target the central enzyme in *DNL* we used IPI-9119, a specific and novel FASN inhibitor (referred to in figure as FASNi) that we previously characterized (18). We show here that FASN blockade leads to DNA damage, a mechanism dependent on increased synthesis of ceramide. This metabolic alteration was exploited by combining FASN and PARP inhibition as a therapeutic strategy for CRPC. BRCAness is achieved by suppressing DNL pharmacologically, which results in downregulation of enzymes involved not only in HR, but also in NHEJ. Taken altogether these findings suggested that FASN inhibitors can potentiate the efficacy of PARP-directed therapy and expand its benefit to HR-competent patients.

RESULTS

Sphingolipid metabolism is modulated by FASN inhibition

Ceramide synthase are central enzymes in the synthesis of ceramide. RNAseq data showed that treatment with the FASN inhibitor (FASNi) induced transcriptional upregulation of genes involved in ceramide metabolism. In LNCaP and C4-2 cells there was an overall upregulation of genes involved *de novo* synthesis of ceramide, while only C4-2 cells showed suppression of genes on the sphingomyelinase pathway; for 22Rv1 cells, no significant modulation of these genes was observed (Figure 1A). To confirm the effect at protein level, we analyzed two central enzymes in ceramide synthesis, ceramide synthase 2 (CERS2) and serine palmitoyltransferase (SPT). Protein analysis confirmed an increase in CERS2, but no effect was seen on SPT with the FASN inhibitor (Figure 1B). Lipid profiling with targeted HILIC LC-MS/MS analysis (Data file S1) showed increased abundance of total ceramide following FASN inhibition (Figure 1C), with modulation of several classes of lipids in LNCaP and C4-2 cells, including ceramide, dihydroceramide, hexosylceramide, lactosylceramide and sphingomyelin, while no modulation was observed in 22Rv1 cells (Figure 1D). Due to the unique response that FASN inhibition elicited in 22Rv1 cells, they were used as control to define the role of sphingolipid metabolism.

Because ceramide synthase can use different fatty acids for the acylation of the sphingoid base, ceramides can show a range of acyl chain length (number of carbon atoms) and unsaturation (number of double bonds) (Figure 2A). To evaluate the effect of FASN inhibition on ceramides, along with total ceramide abundance modulation, we also evaluated the fatty acids used in the acyl chains. We identified an increase in fatty acid acyl chain unsaturation (polyunsaturated fatty acids or PUFAs), as well as chain length in ceramide species. For LNCaP cells, we observed a 5-fold increase in abundance of ceramide with 4 unsaturation, while a 3-fold increase was induced in abundance of ceramide with 22 and 24 carbon. Similarly, for C4-2 cells, we observed a 4-fold increase in abundance of ceramide with 4 unsaturation while a 3- and 5-fold increase was induced in abundance of ceramide with 22 and 24 carbon, respectively. In 22Rv1 cells, we did not detect any significant alteration (Figure 2B,C). The detailed characterization of fatty acid composition of sphingolipids in all the cell lines is reported in Figure S1A. As highly unsaturated and

longer fatty acids can alter the oxidative state of the cells, we evaluated how FASN blockade affected protein and lipid oxidative damage through the analysis of protein carbonylation and lipid peroxidation. We observed a significant increase in abundance of both carbonylated protein and lipid peroxidation in all cell lines, while addition of exogenous palmitate, the product of FASN enzymatic activity, was able to rescue this effect (Figure 2D). Although 22Rv1 cells did not alter sphingolipid metabolism after FASN inhibition, they demonstrated increased fatty acid unsaturation in other lipid classes, such as phosphatidylcholine and phosphatidylethanolamine (Figure S1B), which can also lead to intracellular oxidative damage. When we evaluated the ratio between reduced glutathione (GSH) and oxidized glutathione (GSSG) using untargeted MS-based metabolomics as previously reported (18), we observed that FASNi increases GSH:GSSG ratio, a known marker of redox status, in 22Rv1 but not in LNCaP cells (Figure S1C), suggesting that 22Rv1 cells were either producing less ROS or had a more effective antioxidant response. Our previously published metabolomics and RNAseq data also showed upregulation of cholesterol synthesis after FASN inhibition (18). This suggested that the increase in sphingolipids induced by palmitate depletion was not exclusive, but a survival mechanism triggered by these cells to re-instate neutral lipids.

FASN inhibition downregulates DNA damage response and induces DNA oxidative damage

To evaluate FASN inhibition effect on DNA damage, we analyzed how FASNi treatment affected phosphorylation of H2A histone family member X (γH2ax) at Ser^{139}, a known marker of double-strand breaks in dsDNA (DSB). Following FASNi treatment, abundance of γH2ax increased in LNCaP and C4-2 cells, but not in 22Rv1 (Figure 3A). We also tested TVB-2640 in these cells, a FASN inhibitor that has been evaluated in a first-in-human clinical study (19), and observed similar induction of DSB to that of IPI-9119 (Figure S2A). Nuclear foci formation of γH2ax was also increased, as expected, while foci formation of p53-binding protein 1 (53BP1) was not affected (Figure 3B,C). DNA damage following FASN blockade was confirmed by comet assay, with increased breaking frequency, as measured by percentage of DNA in comet tail, observed in LNCaP and C4-2 cells (Figure S2B). To evaluate if DNA damage was caused by ROS, we assessed the abundance of the oxidized nucleoside of DNA 8-hydroxydeoxyguanosine (8-OHdG), and observed a significant increase in all cells lines after FASN inhibition (Figure 3D,E).

Next, we analyzed the effect of FASN inhibition in 3D organoid models of CRPC (MSK-PCa1, MSK-PCa2 and MSK-PCa3) that show a diverse mutational landscape reflective of that of the prostate cancer they are derived from (20). Multiplex imaging revealed that, in all organoid models tested, there was induction of DSB after FASN blockade, as observed by increased abundance of γH2ax (Figure 4A-F). We also observed decreased growth of organoids with FASNi treatment, as measured by the number of DAPI-positive cells per organoid, in MSK-PCa1 (Figure 4A,B) and MSK-PC3 organoids (Figure 4E,F), while MSK-PCa2 organoids showed only reduction in the amount of proliferative cells, as seen by a decrease in Ki67-positive cells (Figure 4C,D). Cleavage of PARP was induced in MSK-PCa2 and MSK-PCa3 organoids (Figure 4C-F). We also analyzed how the treatment affected phosphorylation of Acetyl-CoA Carboxylase (ACC) at Ser^{79}, as a readout of *de*

novo lipogenesis inhibition. We observed a strong upregulation of the marker in MSK-PCa1 (Figure 4A,B) and MSK-PC3 organoids (Figure 4E,F).

To determine how FASN inhibition affects DNA damage response, we analyzed the expression abundance of enzymes involved in both Homologous Recombination (HR) and Non-Homologous End Joining (NHEJ). Overall, both LNCaP and C4-2 cells showed similar results, with modulation of several markers, such as reduction in phosphorylation of Ataxia-Telangiectasia Mutated (ATM) kinase at Ser^{1981} and reduced abundance of p95/NBS1, Ku70, Ku80 and DNA Ligase IV (Figure 5A,B). Exogenous palmitate was capable of rescuing most of these markers, confirming the role of lipid modulation in suppression of the repair enzymes. In 22Rv1 cells, however, no significant modulation was observed. HR efficiency was evaluated through co-transfection of two plasmids with deletion mutants (dl-1 and dl-2) followed by analysis of the recombination product by qPCR. In line with reduced abundance of the enzymes involved in this pathway, we observed a decreased in HR activity following FASN inhibition (Figure 5C). Next, we checked DNA damage repair response through p53 promoter-based luciferase reporter gene assay and observed a reduction in p53 transcription activity with FASN inhibition, which could be rescued by palmitate addition (Figure 5D). Supporting this finding, protein analysis showed decline in phosphorylation of p53 at Ser^{15} after FASNi treatment, with rescue by palmitate (Figure 5E). Overall, these data indicated that FASN inhibition, and consequent depletion of palmitate, affected DNA damage repair response in prostate cancer cells, inducing oxidative DNA damage and DSB.

DNA damage mediated by FASN inhibition is tied to ceramide synthesis

In order to investigate the role of ceramide metabolism in DNA damage, we targeted *de novo* synthesis of ceramide (Figure 6A) by two approaches: with genetic downregulation of ceramide synthase 2 (CERS2) through siRNA and with myriocin, an inhibitor of serine palmitoyltransferase (SPT). When FASN was inhibited in the presence of CERS2 siRNA, the level of DSB, determined through phosphorylation of γH2ax, was reduced in comparison to FASNi treatment alone, both in LNCaP and C4-2 cells, while no modulation was seen in 22Rv1 cells (Figure 6B).

The level of DSB induced by FASNi was also reduced by myriocin co-treatment in LNCaP cells, although no modulation was observed in the other cell lines (Figure 6C). To verify if SPT inhibition could affect sphingolipid upregulation driven by FASN blockade, we performed lipidomics analysis (Data file S1). A strong reduction in both dihydroceramide and sphingomyelin was seen in LNCaP and C4-2 cells, while modulation of ceramide was seen only in LNCaP cells (Figure 6D). This is in keeping with the fact that DSB rescue with SPT blockade was observed only in this cell line. In addition to the effect on DNA damage, a reduction in protein carbonylation was seen in LNCaP cells co-treated with FASNi and myriocin (Figure 6E). Furthermore, LNCaP and C4-2 cells treated with different concentrations of exogenous long-chain ceramide (C24:1) showed increased phosphorylation of H2ax, while 22Rv1 cells were not affected (Figure 6F). To confirm that the exogenous ceramide was incorporated to the cellular lipid pool, we performed lipid profiling in these cells; as expected, there was a significant increase in total sphingolipid abundance after treatment (Figure S3A). Because our data indicated that ceramide was not

the only lipid class increased with FASN inhibition, as cholesterol was also shown to be upregulated (18), we tested the combined effect of FASNi with simvastatin, an inhibitor of HMG-CoA reductase, the rate-limiting enzyme for cholesterol synthesis. Blocking cholesterol synthesis did not affect phosphorylation of H2ax, neither did it rescue the abundance of p95/NBS1, strengthening the role of ceramide accumulation in driving DNA damage and HR suppression in FASN-inhibited cells (Figure S3B).

Finally, since we previously demonstrated that FASN blockade in LNCaP cells can lead to ER stress and suppress protein translation (18), we evaluated if ceramide could have the same effect. Indeed, treatment with exogenous long-chain ceramide downregulated global protein synthesis, as determined by surface sensing of translation assay (Figure S3C). The reduction in protein synthesis was partially rescued by myriocin (Figure S3D). FASNi treatment did not affect protein synthesis in 22Rv1 cells. These findings suggested that impaired protein synthesis induced by FASN blockade might be dependent on ceramide accumulation, a conclusion that warrants further investigation.

FASN inhibition potentiates PARP inhibitors in prostate cancer cells and 3D organoids

Since a significant downregulation of DNA damage response, particularly HR, was observed in prostate cells subjected to FASN inhibition, we decided to evaluate if FASNi could potentiate therapeutic efficacy of the PARP inhibitor Olaparib. Combination treatment of FASNi with Olaparib showed increased reduction of cell growth in all cells tested, when compared to either agent alone (Figure 7A). Additionally, combined inhibition of FASN and PARP inhibition was able to induce apoptosis of the castration-resistant cells (Figure 7B), while there was an increase in PARP cleavage in LNCaP and C4-2 cells for combination therapy, in C4-2 cells we also observed a potentiated effect in comparison to Olaparib alone (Figure 7C). Increased necrosis was also observed with combination therapy, but only for C4-2 cells (Figure 7B). In hormone sensitive LNCaP cells neither apoptosis nor necrosis were increased with the combined treatment (Figure 7B).

A potentiated PARP inhibition was also observed in 3D organoid models of CRPC. For all organoid models evaluated, we observed reduced organoid diameter (Figure 7D) and cell growth (Figure 7E) with the drug combination treatment than with either drug alone. For MSK-PCa2, however, the cell growth reduction was mostly driven by PARP inhibition effect. Apoptosis and necrosis were also increased when organoids were co-treated with both inhibitors (Figure 7F), although MSK-PCa2 organoids did not show increase in the number of apoptotic or necrotic cells with treatment. An effective response of the FASN and PARP combined therapy was seen across CRPC models of different molecular features.

In summary, while FASN inhibition shut down *de novo* lipogenesis, leading to a decrease in saturated and monounsaturated fatty acids (18), it also increased the synthesis of sphingolipids. These were assembled with unsaturated and long acyl chains, utilizing -PUFAs taken up from the extracellular space. This also led to upregulation of ROS, a known consequence of increased PUFA utilization and their peroxidation, observed both through protein and DNA oxidative damage markers. FASN inhibition resulted in the downregulation of enzymes responsible for homologous recombination, which rendered the DNA damage response less effective, i.e. it induced “BRCAness”. Together, the increased

oxidative damage of DNA and reduced damage repair response led to increased abundance of DSB, which could be leveraged to potentiate the anti-tumor effect of PARP inhibition (Figure 8).

DISCUSSION

This study provides evidence that suppression of *de novo* lipogenesis can induce DNA damage in prostate cancer cells through modulation of sphingolipid metabolism. The crosstalk between sphingolipids and DNA damage is not new. Ceramide synthesis both *de novo* or through the sphingomyelin pathway has been shown to play a role in DNA damage induction and apoptosis, a stress response mechanism regulated by ATM (21, 22). Our data is in line with these findings, as FASN inhibition increased ceramide abundance while impairing ATM autophosphorylation, and consequent activation, on residue Ser^{1981}.

Following FASN inhibition, we observed cell-type specific effects. While LNCaP and C4-2 cells showed upregulation of sphingolipid synthesis, particularly ceramide and dihydroceramide, 22Rv1 cells did not show sphingolipid modulation. Furthermore, the suppression of HR and NHEJ was observed only in LNCaP and C4-2 cells. It is important to note that C4-2 cells are derived from LNCaP, although certain features are different between these lines, particularly androgen dependence (23). While DNA and protein oxidative damage was observed in all cell types tested, this led to DSB accumulation only in LNCaP and C4-2 cells, an effect that could be directly linked to DNA damage repair impairment. The molecular features of the cells analyzed are diverse: all cells express functional P53 (24, 25); while *BRCA1/2* mutations are harbored in both LNCaP and 22Rv1 cells, their response to FASN inhibition is very different (26); C4-2, a line that displays BRCAness in response to FASN inhibition, is *BRCA1* wild-type (27). None of these cells harbor *TMPRSS2-ERG* rearrangement (28), a known sensitizer for PARP inhibition. Finally, both LNCaP and C4-2 are PTEN-negative, while 22Rv1 cells are PTEN-positive (28). Interestingly, the PTEN/PI3K/Akt pathway has been implicated in the modulation of ceramide and sphingomyelin synthesis in glioma cells (29). However, we could not confirm the involvement of this pathway in FASN-induced DNA damage.

Mechanistically, when FASN is inhibited, prostate cancer cells uptake more exogenous lipids as a survival mechanism. These lipids are then stored as neutral lipids, hence the observed increase in ceramide and cholesterol abundance (18). Lipidome remodeling caused by FASNi affects enzymes in the ceramide synthesis pathway both at the transcriptional and post-transcriptional level. While SPT protein amounts were not increased with FASN blockade, SPT pharmacological inhibition decreased ceramide accumulation induced by FASNi. Several metabolic modulators are known to affect SPT activity (30–32), suggesting additional mechanisms might be at play. The increased acyl chain unsaturation of lipid species after FASN inhibition is key in affecting cellular oxidative homeostasis, including the potentiation of DNA damage by ceramide conjugated with PUFA rather than SFA. Studies have previously shown that DNL and saturated membranes support tumor cell growth due to reduced ROS liability and resistance to chemotherapy (33).

Our data supports that FASN inhibition suppresses the DNA damage repair machinery. This is supported by the observed reduced abundance of enzymes involved in HR and NHEJ, reduced P53 and HR activity and unchanged 53BP1 foci, a mediator for DNA repair that promotes NHEJ (34). We showed that FASN inhibition can affect protein synthesis only in cells that also upregulate sphingolipid. The effect on protein synthesis was also observed when cells were treated with exogenous ceramide, suggesting that ER stress induced by FASN blockade is dependent on the abundance of these lipid species. Other studies have shown that ceramide can induce ER stress by disrupting Ca^{2+} homeostasis through inhibition of Sarcoplasmic/endoplasmic reticulum Ca^{2+}- ATPase (SERCA) (35), but the effect of FASN blockade on this enzyme is unknown.

Our group has shown that FASN inhibition can impair AR signaling, reducing AR/AR-V7 abundance as well as downstream targets (18). The AR signaling pathway can also affect the cell response to DNA damage. Androgens can promote DNA repair through DNAPKcs activity while the anti-androgen drug Enzalutamide diminishes DNAPKcs abundance and can potentiate Ionizing Radiation-mediated cell growth reduction (36). Enzalutamide can also promote BRCAness in prostate cancer cells, suppressing HR-associated genes and increasing DNA damage, which can be leveraged as a therapeutic option with PARP blockade in CRPC (37). It is possible that the blockade of FASN activity can downregulate HR/NHEJ and increase DNA damage via AR signaling suppression as well.

Therapeutically, the combined inhibition of PARP and FASN is promising, being effective in cells regardless of *BRCA1/2* mutations or PTEN status. In all cells tested, cell growth inhibition was potentiated by the pharmacologic combination. Our data suggests that this additive effect could be caused by increased oxidative damage induced by depletion of saturated fatty acids. It is important to note that despite different responses in ceramide synthesis, all models tested were similarly affected by FASN and PARP inhibition. Although ceramide upregulation should also play a role in potentiating the anti-tumor effect of PARP inhibitors, other metabolic alterations induced by FASN blockade are also relevant in this context. In the organoid models analyzed, regardless of the diverse background genetic alterations, combined inhibition of FASN and PARP potentiated anti-tumor effect. This was an interesting finding considering the diversity in genomic alteration observed in these models, including in genes involved in DNA damage repair. MSK-PCa2 has a genomic alteration that leads to the complete loss of chromodomain helicase DNA binding protein 1(CHD1), while TP53 mutation and loss of function is reported only for MSK-PCa3. All three organoid lines diverge in mutation status for genes that regulate genomic stability and chromatin remodeling, such as ATRX, MED1 and SETD2 (20).

Combination of PARP and FASN inhibitors can induce non-apoptotic forms of cell death, such as necroptosis and pyroptosis. Necroptosis, in particular, is known to be triggered by RIPK3 following DNA damage (38). In fact, we did not observe increased apoptosis or necrosis in LNCaP cells following FASNi and Olaparib treatment, despite significant reduction in cell proliferation. Further analysis of other forms of cell death is required.

Taken altogether, our data show that FASN activity can be targeted in prostate cancer cells to modulate sphingolipid metabolism and impair the DNA damage repair machinery, with

consequent accumulation of DNA damage. Inhibition of FASN sensitizes prostate cancer models to Olaparib regardless of molecular background, increasing the therapeutic options for prostate cancer patients.

MATERIAL AND METHODS

Reagents

IPI-9119 (Infinity Pharmaceuticals), TVB-2640 (Sagimet Biosciences), Olaparib (Selleck Chemicals), Puromycin (Sigma Aldrich), Palmitate-BSA FAO substrate (Agilent Technologies), Matrigel Matrix Phenol Red Free, LDEV-free (Corning), C24:1 Ceramide [d18:1/24:1] (Cayman Chemical), myriocin from *Mycelia sterilia* (Sigma Aldrich), Simvastatin (Sigma Aldrich).

Cell culture and treatments

Human prostate cell lines, LNCaP (prostate *adenocarcinoma*, lymph node *metastatic* site), 22Rv1 (prostate adenocarcinoma), and C4-2 (androgen-independent human LNCaP prostatic cancer cell subline) were obtained from the American Type Culture Collection (ATCC). Cells were cultured in RPMI 1640, supplemented with 10% fetal bovine serum (FBS), and grown at 37 °C within a humidified atmosphere containing 5% CO_2. All cells were authenticated by ATCC using short tandem repeated profiling and tested routinely for mycoplasma contamination. Cells were not used at passages higher than 50. The following treatments were performed in these cell lines: IPI-9119 treatment at 100 nM in complete medium for 6 days; TVB-2640 treatment at 100 and 250 nM in complete medium for 6 days; Olaparib at 2 μM in complete medium for 6 days and re-added after 72h; BSA-palmitate or BSA at 50 μM in complete medium for 6 days; myriocin at 5 μM in complete medium for 6 days and re-added after 72h; C24:1 ceramide at 10, 50 and 100 μM in complete medium for 6 days and re-added after 72h.

3D Organoid culture

MSK-PCa1, MSK-PCa2, and MSK-PCa3 organoids were gently provided by Yu Chen, Memorial Sloan-Kettering Cancer Center (New York). Organoids were dissociated to single cells with TrypLE and seeded at 2-10 $x10^3$ cells/well, mixed with 20 μL of growth factor reduced matrigel, in a 12-well plate. Organoids were cultured in appropriate medium (20) in the presence of IPI-9119 at 500nM, Olaparib at 2 μM or DMSO for 21 days, with medium replaced every 3 days. Organoid images were captured on a THUNDER imager LEICA DMi8 Microscope (LEICA, Germany), using the software LASx (3.7.4.23463). Organoid diameter analysis was done manually using Image J software (National Institutes of Health).

CERS2 knock-down

Cells were seeded at $1.5x10^5$ cells/well in a 6-well plate and transfected with 50 nM of CERS2 siRNA (Origene SR323951A and SR323951C) or 50 nM of scramble siRNA (Origene SR30004) and DharmaFECT (Horizon Discovery). After 2 hrs of incubation, medium added with either 100 nM IPI-9119 or DMSO. Cells were harvested on the 6th day. The effectiveness of the siRNA knock-down was verified by immunoblotting.

Luciferase assay

Cells were plated at 6.5 x10^5 cells into 60 mm dishes and treated with 100 nM IPI-9119 in the presence of 50 μM BSA-palmitate or BSA only. After 96 hrs of incubation, cells re-seeded at 30,000 cells/well in 96-well plate and transfected with 90 ng of pGL4.38[luc2P/p53 RE] and 10 ng of pGL4.75 [hRluc/CMV] constructs (Promega) using Fugene HD and its manufacturer's recommendations. On day 6, firefly and Renilla luciferase assessed using Dual Luciferase Assay Kit (Promega), according to the manufacturer's protocol. The ratio of p53 reporter luminescence was normalized to control Renilla luminescence.

Apoptosis and necrosis assays

Following 6 days of treatment with 100 nM IPI-9119 with or without 2 μM Olaparib, cells were collected, and viability measured using Vi-Cell BLU automated cell viability counter (Beckman Coulter). Cells were transferred into 96-well plate and apoptosis/necrosis measured using the RealTime-Glo Annexin-V Apoptosis and Necrosis Assay kit (Promega), following the manufacturer's instructions. Apoptosis measured as luminescence through PS:Annexin V binding and necrosis measured as fluorescence (485/525 nm) by cell-impermeant profluorescent DNA dye, with values normalized to total cell numbers.

Cell immunofluorescence

Cells were seeded at 1.5 x10^5/ well in a 6-well plate and treated with 100 nM IPI-9119 or DMSO. On the 4th day, cells were re-seeded at 7500 cells/chamber in 8-chamber glass slides coated with poly-L-lysine. Cells were incubated for additional 48 hours with IPI-9119 or vehicle before fixing in formaldehyde for 15 min at room temperature. Slides were washed with PBS, cell permeabilization performed (0.5% Triton X-100), following by blocking with BSA. Phosphorylated H2A.X (Ser^{139}) (CST, 80312), 53BP1 (CST, 4937), and 8-OHdG (Santa Cruz, sc-393871) antibodies were incubated overnight at 4°C, following by 1-hour incubation with Goat Anti-Rabbit IgG Alexa Fluor 594 (ab150080) and Goat Anti-Mouse Alexa Fluor 488 (ab150113). Slides were mounted in DAPI Antifade Mounting Medium (Vectashield). Imaging was carried out on a THUNDER imager LEICA DMi8 Microscope (LEICA, Germany), using the software LASx (3.7.4.23463). Image quantification data were performed using Image J software (National Institutes of Health).

Immunoblotting

Cell lysates were prepared in RIPA buffer supplemented with proteinase/phosphatase inhibitors. Protein content was quantified using Bradford Protein Assay dye (Bio-Rad) and 15 μg of total lysate resolved in precast tri-glycine gels (Invitrogen) and transferred onto nitrocellulose membranes (GE). The following antibodies were used: p-ATM (Abcam, ab81292); p-P53 (CST, 9286); γH2ax (CST, 9718); P95/NBS1 (CST, 14956); Vinculin (Sigma Aldrich, V9131); p-eIF2a (CST, 9721), Ku80 (CST, 2753); Ku70 (CST, 4588); DNA Ligase IV (CST, 14649); CERS2 (Abcam, ab176709); puromycin (Sigma Aldrich, MABE343); c-PARP (CST, 9541); SPT (Abcam, ab23696); Goat Anti-Rabbit IgG-HRP (Bio-Rad, 1706515); Goat Anti-Mouse IgG-HRP (Bio-Rad, 1706516). Enhanced chemiluminescence substrate (Pierce ECL) was used and blots were acquired in a G;Box

Chemi XRQ gel/blot imager system (Syngene). Marker quantification was done using GeneTools software (Syngene).

Total protein carbonylation

Protein carbonylation abundance was assessed using total protein lysate prepared in RIPA buffer. Derivatization of protein carbonyl groups was done with DNP and determined with ELISA method (39) using anti-DNP (A6430, Molecular Probes 1:2700, 1 h, 37 °C) and HRP-conjugated antibodies. As positive control for protein oxidation, untreated cells were incubated with 100 μM hydrogen peroxide for 1 h.

Protein synthesis (SUnSET assay)

Neosynthesized proteins were evaluated by puromycin incorporation, as previously described for the surface sensing of translation (SUnSET) assay. Briefly, after 6 days of treatment with IPI-9119, myriocin or ceramide, as indicated, cells were incubated with 1 μg/mL of puromycin aminonucleoside (Sigma Aldrich) before being harvested. Cell pellets were lysed in RIPA buffer and 15 μg of total lysate was resolved in precast tri-glycine gels (Invitrogen) and transferred onto nitrocellulose membranes. Puromycin incorporated into protein was detected by immunoblotting with Anti-puromycin antibody (Sigma Aldrich, MABE343).

Lipidomics

Lipidomic profiling was performed by Lipometrix (KU Leuven, Belgium) using their liquid chromatography-electrospray ionization tandem mass spectrometry (LC-ESI/MS/MS) on a Nexera X2 UHPLC system (Shimadzu) coupled with a hybrid triple quadrupole/linear ion trap mass spectrometer (6500+ QTRAP system; AB SCIEX), as described (40).

Metabolomics

Metabolic profiling was performed by Metabolon Inc., using their liquid chromatography-MS platform. Sample preparation, data availability and analysis were previously reported (18).

Comet assay

Single cell gel electrophoresis assay was performed using neutral Comet Assay kit (Trevigen), following manufacturer’s protocol. Briefly, cells treated with IPI-9119 for 6 days were immobilized in low-melting point agarose on glass slides. Following cell lysis, nucleoids were subjected to electrophoresis and stained with SYBR Gold nucleic acid gel stain (ThermoFisher). Comet images were acquired by epifluorescence microscopy (496/522 nm) on THUNDER imager LEICA DMi8 Microscope (LEICA, Germany) at 10X. DNA fragmentation was assessed by the percentage of DNA in the comet tail using CometScore 2.0 software (TriTek), considering a cutoff of 85% and a threshold of 10% for comet probability.

Multiplex Immunofluorescence

Slide staining was done in a Leica BondRX automated tissue stainer via iterative application of the following primary antibodies: γH2ax (Ser^{139}) (CST 9718), Ki67 (CST, 12202), cleaved PARP (Abcam ab32064), phosphorylated ACC (Ser^{79}) (CST, 3661) and Cytokeratin HMW (Leica, 34E12). HRP-conjugated secondary antibodies (polymer) were used, followed by fluorophore-tyramine conjugates to amplify fluorescence signal. Automated Opal 7-Color IHC Kit with 6 reactive fluorophores (Opal 520, Opal 540, Opal 570, Opal 620, Opal 650 and Opal 690) was used. Whole slides were acquired using the Vectra Polaris Automated Quantitative Pathology Imaging System (Akoya Biosciences, Hopkinton, MA). Images were processed by linear spectral unmixing and deconvolved. Cell segmentation and image quantification were performed using HALO (Indica Labs, v3.3.2541, Albuquerque, US).

RNA sequencing

Cells were treated with DMSO or IPI-9119 at 100 nM for 6 days, harvested and washed with PBS. Frozen cell pellets were sent to Azenta Life Sciences (GENEWIZ) for RNAseq analysis. RNA library preparation was performed with polyA selection followed by sequencing with Illumina HiSeq 2x150bp. Paired-end reads were quality trimmed using Trimmomatic v.0.36 and subsequently mapped to the Homo sapiens GRCh38 reference genome available on ENSEMBL using the STAR aligner v.2.5.2b. Gene hit counts were quantified by featureCounts from the Subread package v.1.5.2. Differential gene expression was performed by DESeq2. Normalized gene hit counts were used to calculate Log_2FoldChange of mRNA abundance of IPI-treated vs DMSO-treated cells.

Lipid peroxidation analysis

Following 6 days of treatment with IPI-9119 in the presence of 50 μM BSA-palmitate or BSA only, cells were harvested, washed with fresh medium and incubated with 5 μM of the lipid peroxidation sensor BODIPY™ 581/591 C11 (ThermoFisher) at 37°C for 30 minutes. Cells were then washed with PBS and resuspended in fresh phenol-free medium, transfer into a 96-well plate, and the shift of the fluorescence emission peak was assessed by reading the excitation/emission of the probe at 571/591 nm and at 488/510 nm. Ratio of oxidized/reduced probe was normalized to total viable cells.

Homologous Recombination activity

HR assay was assessed with the HR Assay Kit following manufacturer's instructions (Norgen Biotek Corp). Briefly, cells were treated with 100 nM of IPI-9119 for 5 days and then co-transfected with 500 ng of two plasmids containing deletion mutants (dl-1 and dl-2), in the presence of FuGENE HD (Promega). Twenty-four hours after transfection, DNA was isolated with Purelink Genomic DNA kit (Invitrogen). HR efficiency was assessed by qPCR, using primer mixtures provided with the kit to amplify the homologous recombination product (assay primers) and the dl plasmids backbone (universal primers). The Luna Universal qPCR Master Mix (New England Biolabs) was used with the QuantStudio™ 5 Real-Time PCR Instrument (ThermoFisher) and the Comparative Ct (ΔΔCt) method, using universal primer product as reference.

Analysis

For Statistical analyses, GraphPad Prism 9 was used. For mean comparisons between control and IPI-9119, analysis done by unpaired t-test or multiple unpaired t-tests. Multiplicity adjusted P values (q) reported for multiple t-tests. Multiple comparisons were done by one-way ANOVA with Tukey's multiple comparison test, adjusted P values were reported. Multiple independent comparisons were done by two-way ANOVA with Šídák's or Dunnett's multiple comparison test, adjusted P values were reported. For lipidomics analysis, peak integration done with MultiQuantTM 3.0.3, lipid species signals corrected for isotopic contributions with Python Molmass 2019.1.1 and quantified based on internal standard signals and adheres to the guidelines of the Lipidomics Standards Initiative (LSI) (level 2 type quantification as defined by the LSI). Counts were then normalized to DNA content. Heat-map of lipid and transcriptional profiling were done using Heatmapper (41), by using normalized values of indicated lipid class summed based on the acyl chain fatty acid or normalized mRNA counts, respectively.

Supplementary Material

Refer to Web version on PubMed Central for supplementary material.

Acknowledgments

We thank Dr Johan Swinnen and the Lipometrix team at KU Leuven for providing advanced lipidomics services with their state-of-the-art platform. We thank Dr Tania Pannellini, and the Multiparametric In Situ Imaging (MISI) Laboratory team for assistance with multiplex staining and multi-spectral imaging. We thank Dr Yu Chen from Memorial Sloan-Kettering Cancer Center for kindly providing us with the 3D organoid models MSK-PCa1, MSK-PCa2 and MSK-PCa3. ML has an appointment at Dana-Farber Cancer Institute, Harvard Medical School and is Professor of Pathology, Emeritus, Harvard Medical School

Funding

This work was supported by the following awards:

Department of Defense (DoD) - Awards W81XWH-17-1-0483; W81XWH-19-1-0566 to M.L.,

Prostate Cancer Foundation (PCF) – Challenge Award 22Chal05

National Institutes of Health (NIH) - Award P50 CA211024 and Award R01 CA131945 to M.L.

Award PC150263 and Claudia Adams Barr Award in Innovative Basic Cancer Research (DFCI) to G.Z.

Data and materials availability

All data needed to evaluate the conclusions in the paper are present in the paper or the Supplementary Materials. RNAseq data has been deposited in the Gene Expression Omnibus (GEO) database (GSE114016 and GSE224323). Normalized lipidomics data is provided in supplementary material (Data file S1).

REFERENCES

1. Swinnen JV, Roskams T, Joniau S, Van Poppel H, Oyen R, Baert L, Heyns W, Verhoeven G, Overexpression of fatty acid synthase is an early and common event in the development of prostate cancer. Int J Cancer 98, 19–22 (2002); published online EpubMar 01 (10.1002/ijc.10127). [PubMed: 11857379]

2. Migita T, Ruiz S, Fornari A, Fiorentino M, Priolo C, Zadra G, Inazuka F, Grisanzio C, Palescandolo E, Shin E, Fiore C, Xie W, Kung AL, Febbo PG, Subramanian A, Mucci L, Ma J, Signoretti S, Stampfer M, Hahn WC, Finn S, Loda M, Fatty acid synthase: a metabolic enzyme and candidate oncogene in prostate cancer. J Natl Cancer Inst 101, 519–532 (2009); published online EpubApr (10.1093/jnci/djp030). [PubMed: 19318631]

3. Shurbaji MS, Kalbfleisch JH, Thurmond TS, Immunohistochemical detection of a fatty acid synthase (OA-519) as a predictor of progression of prostate cancer. Hum Pathol 27, 917–921 (1996); published online EpubSep (10.1016/s0046-8177(96)90218-x). [PubMed: 8816886]

4. Zadra G, Photopoulos C, Loda M, The fat side of prostate cancer. Biochim Biophys Acta 1831, 1518–1532 (2013); published online EpubOct (10.1016/j.bbalip.2013.03.010). [PubMed: 23562839]

5. Swinnen JV, Heemers H, van de Sande T, de Schrijver E, Brusselmans K, Heyns W, Verhoeven G, Androgens, lipogenesis and prostate cancer. J Steroid Biochem Mol Biol 92, 273–279 (2004); published online EpubNov (10.1016/j.jsbmb.2004.10.013). [PubMed: 15663990]

6. Ettinger SL, Sobel R, Whitmore TG, Akbari M, Bradley DR, Gleave ME, Nelson CC, Dysregulation of sterol response element-binding proteins and downstream effectors in prostate cancer during progression to androgen independence. Cancer Res 64, 2212–2221 (2004); published online EpubMar (10.1158/0008-5472.can-2148-2). [PubMed: 15026365]

7. Reginato A, Veras ACC, Baqueiro MDN, Panzarin C, Siqueira BP, Milanski M, Lisboa PC, Torsoni AS, The Role of Fatty Acids in Ceramide Pathways and Their Influence on Hypothalamic Regulation of Energy Balance: A Systematic Review. Int J Mol Sci 22, (2021); published online EpubMay 19 (10.3390/ijms22105357).

8. Levy M, Futerman AH, Mammalian ceramide synthases. IUBMB Life 62, 347–356 (2010); published online EpubMay (10.1002/iub.319). [PubMed: 20222015]

9. Chatterjee N, Walker GC, Mechanisms of DNA damage, repair, and mutagenesis. Environ Mol Mutagen 58, 235–263 (2017); published online EpubJun (10.1002/em.22087). [PubMed: 28485537]

10. Robson M, Im SA, Senkus E, Xu B, Domchek SM, Masuda N, Delaloge S, Li W, Tung N, Armstrong A, Wu W, Goessl C, Runswick S, Conte P, Olaparib for Metastatic Breast Cancer in Patients with a Germline BRCA Mutation. N Engl J Med 377, 523–533 (2017); published online EpubAug 10 (10.1056/NEJMoa1706450). [PubMed: 28578601]

11. Ledermann J, Harter P, Gourley C, Friedlander M, Vergote I, Rustin G, Scott CL, Meier W, Shapira-Frommer R, Safra T, Matei D, Fielding A, Spencer S, Dougherty B, Orr M, Hodgson D, Barrett JC, Matulonis U, Olaparib maintenance therapy in patients with platinum-sensitive relapsed serous ovarian cancer: a preplanned retrospective analysis of outcomes by BRCA status in a randomised phase 2 trial. Lancet Oncol 15, 852–861 (2014); published online EpubJul (10.1016/S1470-2045(14)70228-1). [PubMed: 24882434]

12. Golan T, Hammel P, Reni M, Van Cutsem E, Macarulla T, Hall MJ, Park JO, Hochhauser D, Arnold D, Oh DY, Reinacher-Schick A, Tortora G, Algul H, O'Reilly EM, McGuinness D, Cui KY, Schlienger K, Locker GY, Kindler HL, Maintenance Olaparib for Germline BRCA-Mutated Metastatic Pancreatic Cancer. N Engl J Med 381, 317–327 (2019); published online EpubJul 25 (10.1056/NEJMoa1903387). [PubMed: 31157963]

13. de Bono J, Mateo J, Fizazi K, Saad F, Shore N, Sandhu S, Chi KN, Sartor O, Agarwal N, Olmos D, Thiery-Vuillemin A, Twardowski P, Mehra N, Goessl C, Kang J, Burgents J, Wu W, Kohlmann A, Adelman CA, Hussain M, Olaparib for Metastatic Castration-Resistant Prostate Cancer. N Engl J Med 382, 2091–2102 (2020); published online EpubMay 28 (10.1056/NEJMoa1911440). [PubMed: 32343890]

14. Abida W, Patnaik A, Campbell D, Shapiro J, Bryce AH, McDermott R, Sautois B, Vogelzang NJ, Bambury RM, Voog E, Zhang J, Piulats JM, Ryan CJ, Merseburger AS, Daugaard G, Heidenreich A, Fizazi K, Higano CS, Krieger LE, Sternberg CN, Watkins SP, Despain D, Simmons AD, Loehr A, Dowson M, Golsorkhi T, Chowdhury S, investigators T, Rucaparib in Men With Metastatic Castration-Resistant Prostate Cancer Harboring a BRCA1 or BRCA2 Gene Alteration. J Clin Oncol 38, 3763–3772 (2020); published online EpubNov 10 (10.1200/JCO.20.01035). [PubMed: 32795228]

15. Abida W, Armenia J, Gopalan A, Brennan R, Walsh M, Barron D, Danila D, Rathkopf D, Morris M, Slovin S, McLaughlin B, Curtis K, Hyman DM, Durack JC, Solomon SB, Arcila ME, Zehir A, Syed A, Gao J, Chakravarty D, Vargas HA, Robson ME, Joseph V, Offit K, Donoghue MTA,

Abeshouse AA, Kundra R, Heins ZJ, Penson AV, Harris C, Taylor BS, Ladanyi M, Mandelker D, Zhang L, Reuter VE, Kantoff PW, Solit DB, Berger MF, Sawyers CL, Schultz N, Scher HI, Prospective Genomic Profiling of Prostate Cancer Across Disease States Reveals Germline and Somatic Alterations That May Affect Clinical Decision Making. JCO Precis Oncol 2017, (2017); published online EpubJul (10.1200/PO.17.00029).

16. Brenner JC, Ateeq B, Li Y, Yocum AK, Cao Q, Asangani IA, Patel S, Wang X, Liang H, Yu J, Palanisamy N, Siddiqui J, Yan W, Cao X, Mehra R, Sabolch A, Basrur V, Lonigro RJ, Yang J, Tomlins SA, Maher CA, Elenitoba-Johnson KS, Hussain M, Navone NM, Pienta KJ, Varambally S, Feng FY, Chinnaiyan AM, Mechanistic rationale for inhibition of poly(ADP-ribose) polymerase in ETS gene fusion-positive prostate cancer. Cancer Cell 19, 664–678 (2011); published online EpubMay 17 (10.1016/j.ccr.2011.04.010). [PubMed: 21575865]
17. Mansour WY, Tennstedt P, Volquardsen J, Oing C, Kluth M, Hube-Magg C, Borgmann K, Simon R, Petersen C, Dikomey E, Rothkamm K, Loss of PTEN-assisted G2/M checkpoint impedes homologous recombination repair and enhances radio-curability and PARP inhibitor treatment response in prostate cancer. Sci Rep 8, 3947 (2018); published online EpubMar 2 (10.1038/s41598-018-22289-7). [PubMed: 29500400]
18. Zadra G, Ribeiro CF, Chetta P, Ho Y, Cacciatore S, Gao X, Syamala S, Bango C, Photopoulos C, Huang Y, Tyekucheva S, Bastos DC, Tchaicha J, Lawney B, Uo T, D'Anello L, Csibi A, Kalekar R, Larimer B, Ellis L, Butler LM, Morrissey C, McGovern K, Palombella VJ, Kutok JL, Mahmood U, Bosari S, Adams J, Peluso S, Dehm SM, Plymate SR, Loda M, Inhibition of de novo lipogenesis targets androgen receptor signaling in castration-resistant prostate cancer. Proc Natl Acad Sci U S A 116, 631–640 (2019); published online Epub01 (10.1073/pnas.1808834116). [PubMed: 30578319]
19. Falchook G, Infante J, Arkenau HT, Patel MR, Dean E, Borazanci E, Brenner A, Cook N, Lopez J, Pant S, Frankel A, Schmid P, Moore K, McCulloch W, Grimmer K, O'Farrell M, Kemble G, Burris H, First-in-human study of the safety, pharmacokinetics, and pharmacodynamics of first-in-class fatty acid synthase inhibitor TVB-2640 alone and with a taxane in advanced tumors. EClinicalMedicine 34, 100797 (2021); published online EpubApr (10.1016/j.eclinm.2021.100797). [PubMed: 33870151]
20. Gao D, Vela I, Sboner A, Iaquinta PJ, Karthaus WR, Gopalan A, Dowling C, Wanjala JN, Undvall EA, Arora VK, Wongvipat J, Kossai M, Ramazanoglu S, Barboza LP, Di W, Cao Z, Zhang QF, Sirota I, Ran L, MacDonald TY, Beltran H, Mosquera JM, Touijer KA, Scardino PT, Laudone VP, Curtis KR, Rathkopf DE, Morris MJ, Danila DC, Slovin SF, Solomon SB, Eastham JA, Chi P, Carver B, Rubin MA, Scher HI, Clevers H, Sawyers CL, Chen Y, Organoid cultures derived from patients with advanced prostate cancer. Cell 159, 176–187 (2014); published online EpubSep (10.1016/j.cell.2014.08.016). [PubMed: 25201530]
21. Santana P, Pena LA, Haimovitz-Friedman A, Martin S, Green D, McLoughlin M, Cordon-Cardo C, Schuchman EH, Fuks Z, Kolesnick R, Acid sphingomyelinase-deficient human lymphoblasts and mice are defective in radiation-induced apoptosis. Cell 86, 189–199 (1996); published online EpubJul 26 (10.1016/s0092-8674(00)80091-4). [PubMed: 8706124]
22. Liao WC, Haimovitz-Friedman A, Persaud RS, McLoughlin M, Ehleiter D, Zhang N, Gatei M, Lavin M, Kolesnick R, Fuks Z, Ataxia telangiectasia-mutated gene product inhibits DNA damage-induced apoptosis via ceramide synthase. J Biol Chem 274, 17908–17917 (1999); published online EpubJun 18 (10.1074/jbc.274.25.17908). [PubMed: 10364237]
23. Liu AY, Brubaker KD, Goo YA, Quinn JE, Kral S, Sorensen CM, Vessella RL, Belldegrun AS, Hood LE, Lineage relationship between LNCaP and LNCaP-derived prostate cancer cell lines. Prostate 60, 98–108 (2004); published online EpubJul 1 (10.1002/pros.20031). [PubMed: 15162376]
24. Skjoth IH, Issinger OG, Profiling of signaling molecules in four different human prostate carcinoma cell lines before and after induction of apoptosis. Int J Oncol 28, 217–229 (2006); published online EpubJan ([PubMed: 16327999]
25. Liu C, Zhu Y, Lou W, Nadiminty N, Chen X, Zhou Q, Shi XB, deVere White RW, Gao AC, Functional p53 determines docetaxel sensitivity in prostate cancer cells. Prostate 73, 418–427 (2013); published online EpubMar (10.1002/pros.22583). [PubMed: 22996738]

26. Feiersinger GE, Trattnig K, Leitner PD, Guggenberger F, Oberhuber A, Peer S, Hermann M, Skvortsova I, Vrbkova J, Bouchal J, Culig Z, Santer FR, Olaparib is effective in combination with, and as maintenance therapy after, first-line endocrine therapy in prostate cancer cells. Mol Oncol 12, 561–576 (2018); published online EpubApr (10.1002/1878-0261.12185). [PubMed: 29465803]
27. Li J, Wang R, Kong Y, Broman MM, Carlock C, Chen L, Li Z, Farah E, Ratliff TL, Liu X, Targeting Plk1 to Enhance Efficacy of Olaparib in Castration-Resistant Prostate Cancer. Mol Cancer Ther 16, 469–479 (2017); published online EpubMar (10.1158/1535-7163.MCT-16-0361). [PubMed: 28069876]
28. Hong Z, Zhang W, Ding D, Huang Z, Yan Y, Cao W, Pan Y, Hou X, Weroha SJ, Karnes RJ, Wang D, Wu Q, Wu D, Huang H, DNA Damage Promotes TMPRSS2-ERG Oncoprotein Destruction and Prostate Cancer Suppression via Signaling Converged by GSK3beta and WEE1. Mol Cell 79, 1008–1023 e1004 (2020); published online EpubSep 17 (10.1016/j.molcel.2020.07.028). [PubMed: 32871104]
29. Giussani P, Brioschi L, Bassi R, Riboni L, Viani P, Phosphatidylinositol 3-kinase/AKT pathway regulates the endoplasmic reticulum to golgi traffic of ceramide in glioma cells: a link between lipid signaling pathways involved in the control of cell survival. J Biol Chem 284, 5088–5096 (2009); published online EpubFeb 20 (10.1074/jbc.M808934200). [PubMed: 19103588]
30. Perry RJ, Ridgway ND, The role of de novo ceramide synthesis in the mechanism of action of the tricyclic xanthate D609. J Lipid Res 45, 164–173 (2004); published online EpubJan (10.1194/jlr.M300300-JLR200). [PubMed: 13130125]
31. Perry DK, Carton J, Shah AK, Meredith F, Uhlinger DJ, Hannun YA, Serine palmitoyltransferase regulates de novo ceramide generation during etoposide-induced apoptosis. J Biol Chem 275, 9078–9084 (2000); published online EpubMar 24 (10.1074/jbc.275.12.9078). [PubMed: 10722759]
32. Memon RA, Holleran WM, Moser AH, Seki T, Uchida Y, Fuller J, Shigenaga JK, Grunfeld C, Feingold KR, Endotoxin and cytokines increase hepatic sphingolipid biosynthesis and produce lipoproteins enriched in ceramides and sphingomyelin. Arterioscler Thromb Vasc Biol 18, 1257–1265 (1998); published online EpubAug (10.1161/01.atv.18.8.1257). [PubMed: 9714132]
33. Rysman E, Brusselmans K, Scheys K, Timmermans L, Derua R, Munck S, Van Veldhoven PP, Waltregny D, Daniëls VW, Machiels J, Vanderhoydonc F, Smans K, Waelkens E, Verhoeven G, Swinnen JV, De novo lipogenesis protects cancer cells from free radicals and chemotherapeutics by promoting membrane lipid saturation. Cancer Res 70, 8117–8126 (2010); published online EpubOct (10.1158/0008-5472.CAN-09-3871). [PubMed: 20876798]
34. Gupta A, Hunt CR, Chakraborty S, Pandita RK, Yordy J, Ramnarain DB, Horikoshi N, Pandita TK, Role of 53BP1 in the regulation of DNA double-strand break repair pathway choice. Radiat Res 181, 1–8 (2014); published online EpubJan (10.1667/RR13572.1). [PubMed: 24320053]
35. Liu Z, Xia Y, Li B, Xu H, Wang C, Liu Y, Li Y, Li C, Gao N, Li L, Induction of ER stress-mediated apoptosis by ceramide via disruption of ER Ca(2+) homeostasis in human adenoid cystic carcinoma cells. Cell Biosci 4, 71 (2014)10.1186/2045-3701-4-71). [PubMed: 25937892]
36. Goodwin JF, Schiewer MJ, Dean JL, Schrecengost RS, de Leeuw R, Han S, Ma T, Den RB, Dicker AP, Feng FY, Knudsen KE, A hormone-DNA repair circuit governs the response to genotoxic insult. Cancer Discov 3, 1254–1271 (2013); published online EpubNov (10.1158/2159-8290.CD-13-0108). [PubMed: 24027197]
37. Li L, Karanika S, Yang G, Wang J, Park S, Broom BM, Manyam GC, Wu W, Luo Y, Basourakos S, Song JH, Gallick GE, Karantanos T, Korentzelos D, Azad AK, Kim J, Corn PG, Aparicio AM, Logothetis CJ, Troncoso P, Heffernan T, Toniatti C, Lee HS, Lee JS, Zuo X, Chang W, Yin J, Thompson TC, Androgen receptor inhibitor-induced “BRCAness” and PARP inhibition are synthetically lethal for castration-resistant prostate cancer. Sci Signal 10, (2017); published online EpubMay 23 (10.1126/scisignal.aam7479).
38. Tait SW, Ichim G, Green DR, Die another way--non-apoptotic mechanisms of cell death. J Cell Sci 127, 2135–2144 (2014); published online EpubMay 15 (10.1242/jcs.093575). [PubMed: 24833670]
39. Buss H, Chan TP, Sluis KB, Domigan NM, Winterbourn CC, Protein carbonyl measurement by a sensitive ELISA method. Free Radic Biol Med 23, 361–366 (1997)10.1016/s0891-5849(97)00104-4). [PubMed: 9214571]

40. Butler LM, Mah CY, Machiels J, Vincent AD, Irani S, Mutuku SM, Spotbeen X, Bagadi M, Waltregny D, Moldovan M, Dehairs J, Vanderhoydonc F, Bloch K, Das R, Stahl J, Kench JG, Gevaert T, Derua R, Waelkens E, Nassar ZD, Selth LA, Trim PJ, Snel MF, Lynn DJ, Tilley WD, Horvath LG, Centenera MM, Swinnen JV, Lipidomic Profiling of Clinical Prostate Cancer Reveals Targetable Alterations in Membrane Lipid Composition. Cancer Res 81, 4981–4993 (2021); published online EpubOct 1 (10.1158/0008-5472.CAN-20-3863). [PubMed: 34362796]

41. Babicki S, Arndt D, Marcu A, Liang Y, Grant JR, Maciejewski A, Wishart DS, Heatmapper: web-enabled heat mapping for all. Nucleic Acids Res 44, W147–153 (2016); published online EpubJul 8 (10.1093/nar/gkw419). [PubMed: 27190236]

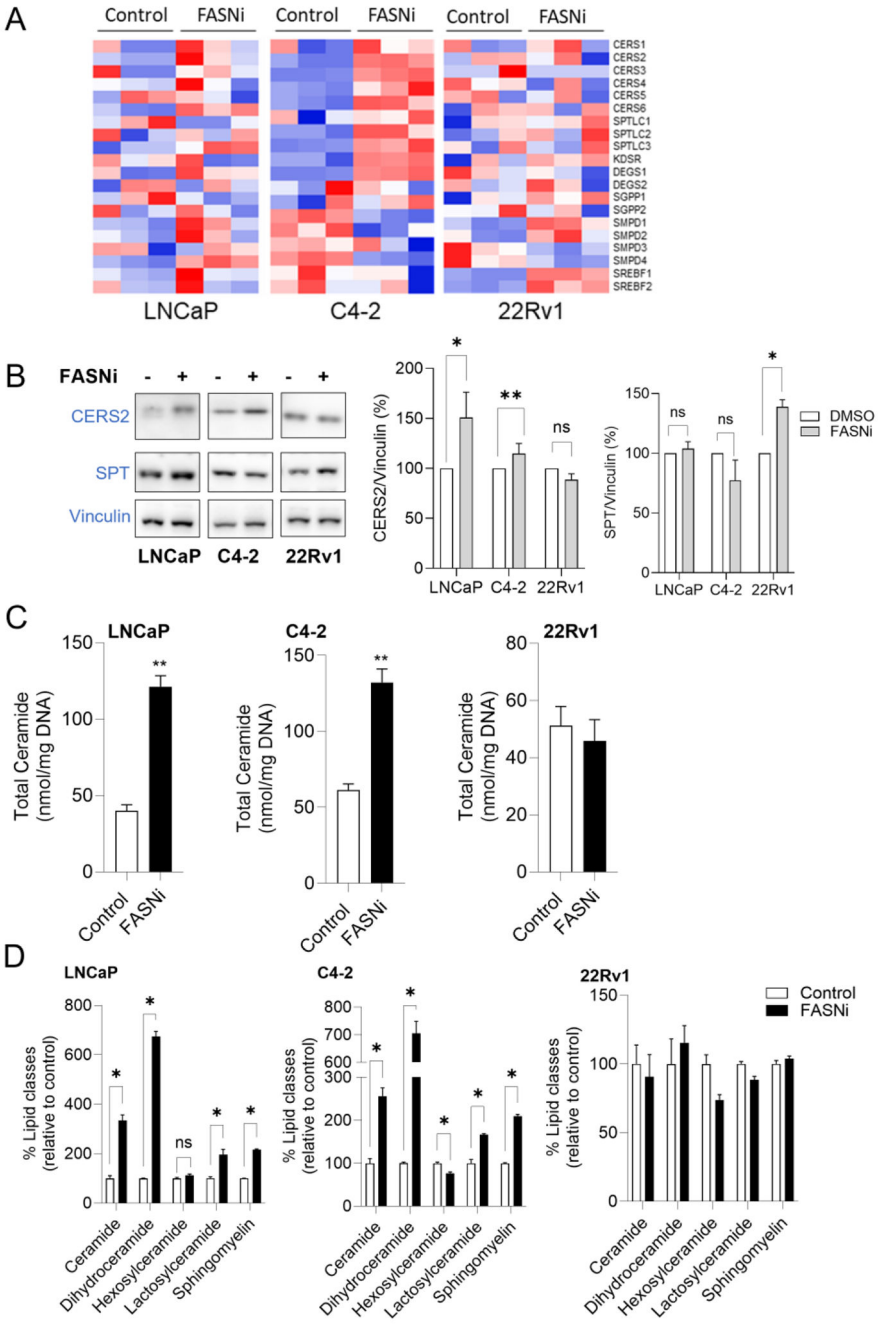

Figure 1. FASN inhibition and sphingolipid metabolism.

(A) Heatmap of transcriptional regulation of genes involved in *de novo* synthesis of ceramide, salvage or sphingomyelinase pathways after FASNi treatment. Normalized counts are shown (n=3 biological replicates). Multiple unpaired t-tests, significant differential values reported as * $p<0.05$. (B) Representative immunoblotting with densitometric analysis (right) of Ceramide Synthase 2 (CERS2) and Serine Palmitoyltransferase (SPT) amounts in cells treated with FASNi. Data plotted as % relative to control of normalized marker expression (marker/vinculin) (n= 3 biological replicates, Mean ± SEM). Multiple unpaired

t-tests, *q<0.05, **q<0.01.(C) Total ceramide amounts after FASN inhibition. Lipid amounts are shown as sum notation of ceramide, dihydroceramide, hexosylceramides and lactosylceramides, expressed as nmol/mg of DNA (n=3 biological replicates, mean ± SEM). Unpaired t-test, **p<0.01. (D) Presence of sphingolipid species after FASN blockade. Total combined sum compositions of indicated lipid classes is shown as % relative to control (n=3 biological replicates, mean ± SEM). Multiple unpaired t-tests, *q<0.05.

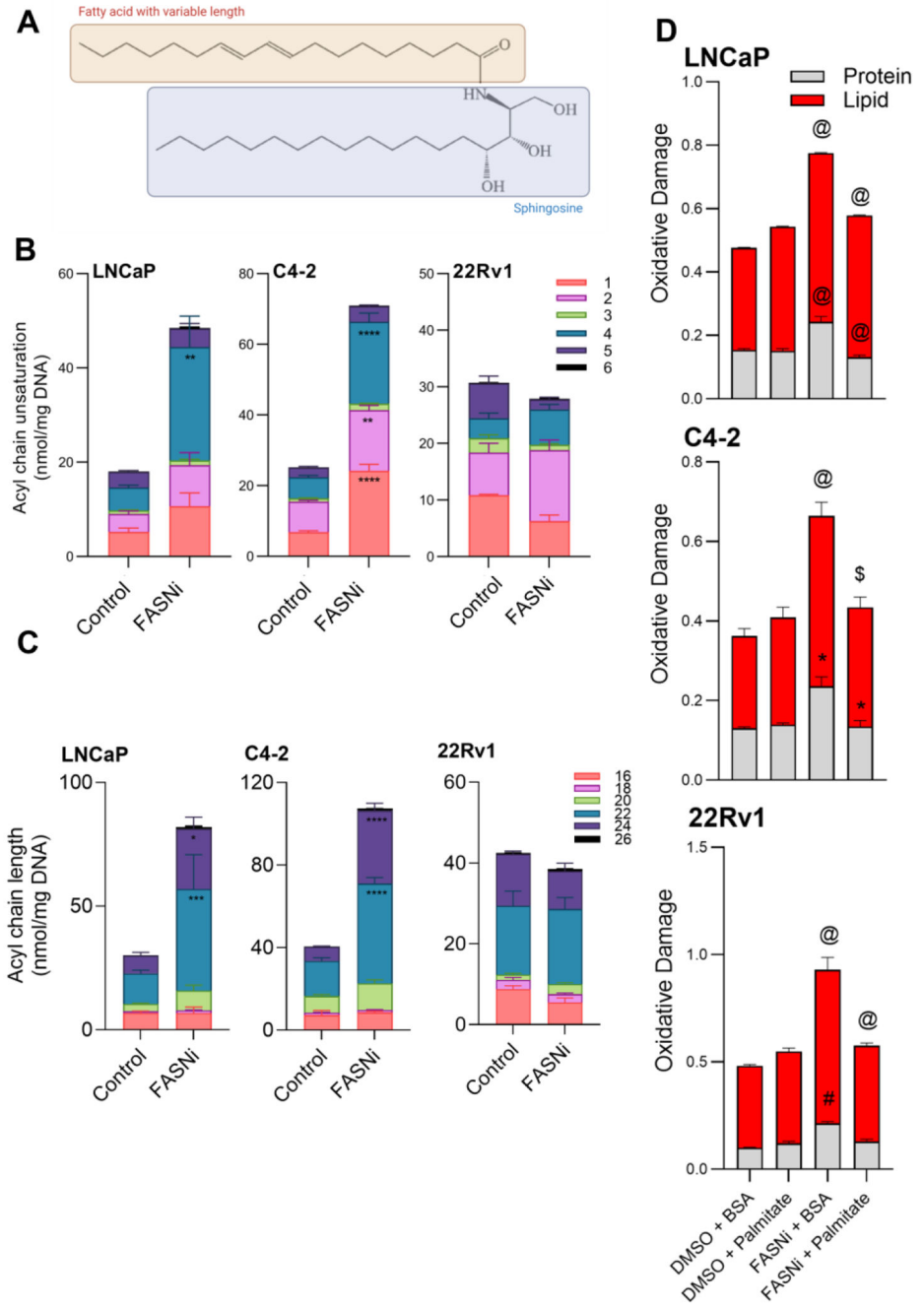

Figure 2. Depletion of palmitate and its effect on ceramide acyl chain unsaturation and length.

(A) Representative chemical structure of ceramide, consisting of a sphingosine and a fatty acid residue that can vary in length and unsaturation level. (B) Number of acyl chain unsaturation in ceramides after FASNi treatment. Ceramides containing fatty acids with the same number of unsaturations (1 to 6) were summed together, data expressed as nmol/mg of DNA (n=3 biological replicates, mean ± SEM). Two-way ANOVA with Šídák's test, **p<0.01, ****p<0.0001. (C) Carbon length of acyl chain in ceramides following FASNi treatment. Ceramides containing fatty acids with the same chain length (16 to 26) were

summed together, data expressed as nmol/mg of DNA (n=3 biological replicates, mean ± SEM). Two-way ANOVA with Šídák's test, *p<0.05, **p<0.01, ****p<0.0001. (D) Oxidative damage of protein and lipid assessed after FASNi treatment combined with palmitate rescue. Results for protein carbonylation are expressed as normalized absorbance at 450 nm (n=12 replicates over 3 independent experiments, mean ± SEM). Lipid oxidative results are expressed as normalized ratio of fluorescence of the reduced to the oxidized probe (n=12 replicates over 3 independent experiments, mean ± SEM). Two-way ANOVA with Tukey's test, * p<0.05, # p<0.01, $ p<0.001, @ p<0.0001.

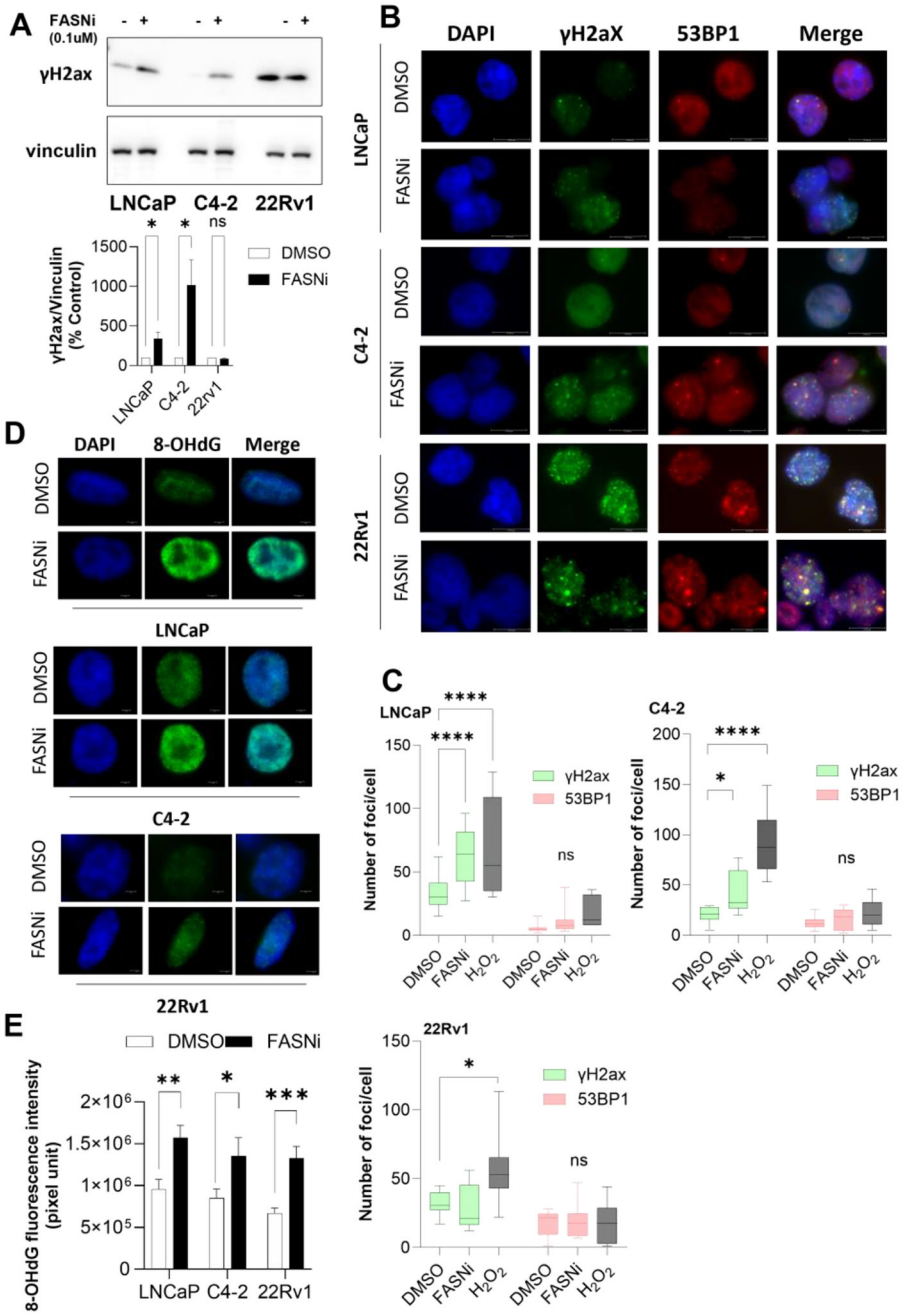

Figure 3. FASN inhibition and DNA oxidative damage.

(A) Representative immunoblotting and densitometric analysis (bottom) of DSB marker, phosphorylated-Histone H2A.X (Ser^{139}) (γH2ax) in cells treated with FASNi. Data plotted as % relative to control of normalized marker expression (n=4-6 biological replicates, Mean ± SEM). Multiple unpaired t-tests, *q<0.05. (B) Representative immunofluorescence of γH2ax (green), 53BP1 (red) and DAPI (blue) in cells treated with FASNi. Scale bar of 15.04 μm. (C) Quantification of γH2ax and 53BP1 foci number per cell (n=20 cells over 3 independent experiments, Min to Max). Positive control (hydrogen peroxide) shown as gray

bars. Two-way ANOVA with Dunnett's test, *p<0.05, ****p<0.0001. (D) Representative immunofluorescence of 8-OHdG (green) and DAPI (blue) in cells treated with FASNi. Images acquired at 40X, scale bar of 3 μm. (E) Quantification of 8-OHdG nuclear fluorescence. Data shown as corrected total nuclear fluorescence (CTNF) normalized to the nuclear area (n=10 cells over 3 independent experiments, mean ± SEM). Multiple unpaired t-test, *q<0.05, **q<0.01, ***q<0.001.

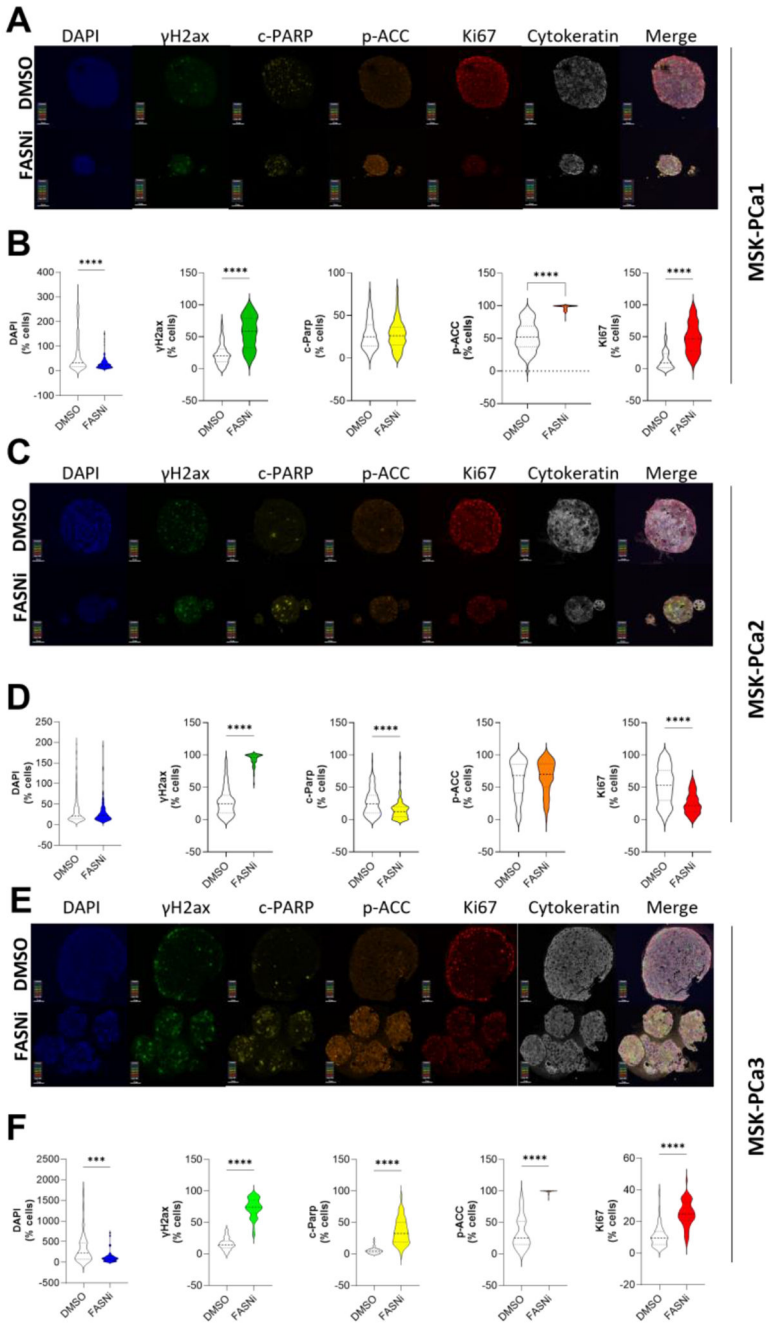

Figure 4. FASN inhibition and DNA damage in 3D organoid models of CRPC.

(A) Representative multiplex immunofluorescence of phosphorylated-Histone H2A.X (Ser^{139}) (γH2ax), cleaved-PARP (c-PARP), phosphorylated Acetyl-CoA Carboxylase (Ser^{79}) (p-ACC), Ki67 and Cytokeratin HMW in MSK-PCa1 organoids treated with FASNi. Scale bar of 50 μm (n=3 independent experiments). (B) Individual marker expression quantification analysis of MSK-PCa1 after FASNi treatment. Whole slide scanned computationally under the same parameters and marker intensity calculated using Halo Image Analysis Platform (Indica Labs). Data shown as % of positively stained

cells (organoids analyzed n=94 for DMSO and n=131 for FASNi, over 3 independent experiments, violin plots). Unpaired t-test, ****p<0.0001. (C) Representative multiplex immunofluorescence of γH2ax, c-PARP, p-ACC, Ki67 and Cytokeratin HMW (n=3 independent experiments) and (D) individual marker expression quantification analysis of MSK-PCa2 organoids after FASNi treatment. Data shown as % of positively stained cells (organoids analyzed n=184 for DMSO and n=95 for FASNi, over 3 independent experiments, violin plots). Unpaired t-test, ****p<0.0001. (E) Representative multiplex immunofluorescence of γH2ax, c-PARP, p-ACC, Ki67 and Cytokeratin HMW (n=3 independent experiments) and (F) individual marker expression quantification analysis of MSK-PCa3 organoids after FASNi treatment. Data shown as % of positively stained cells (organoids analyzed n=41 for DMSO and n=48 for FASNi, over 3 independent experiments, violin plots). Unpaired t-test, ***p<0.001, ****p<0.0001.

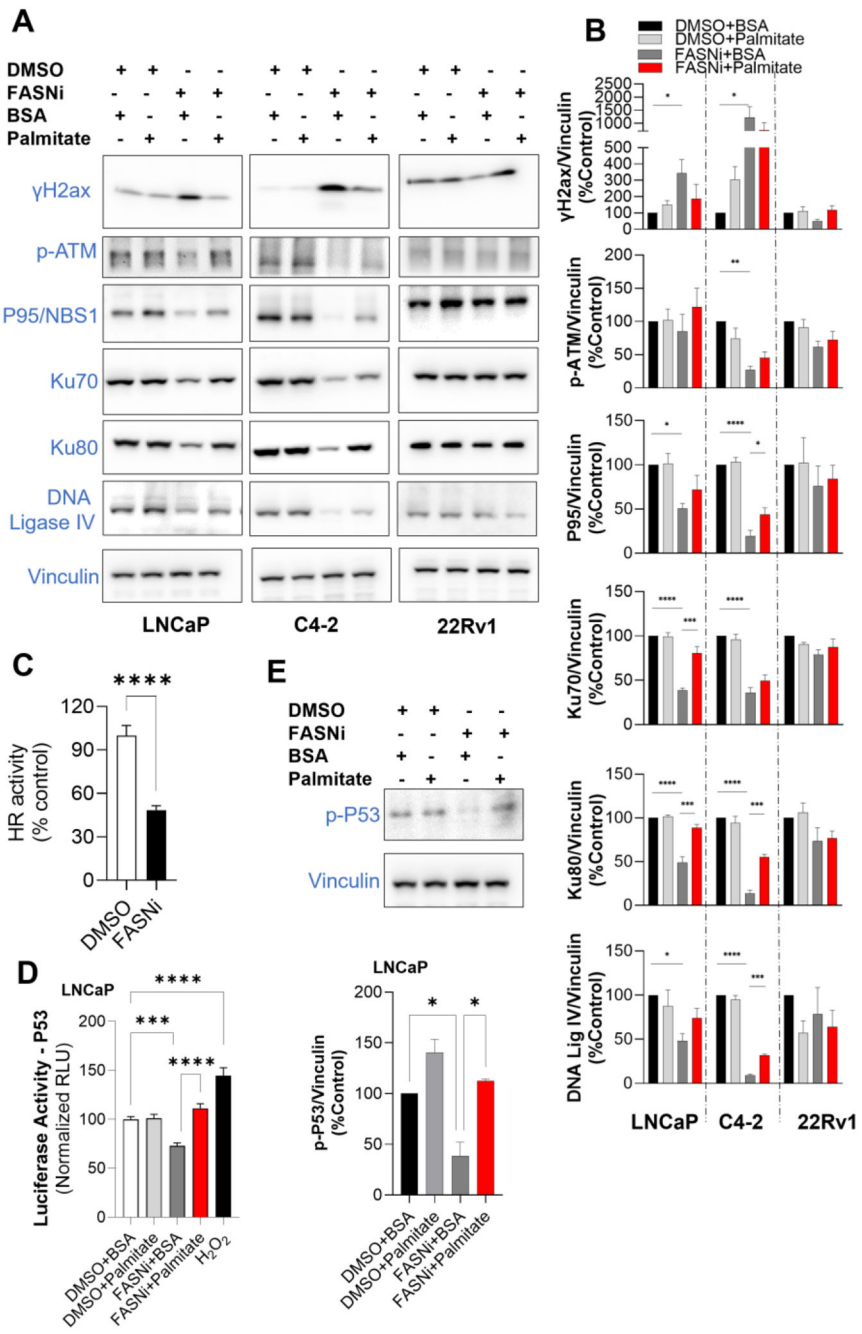

Figure 5. DNA damage repair pathways HR and NHEJ following FASN blockade.

(A) Representative immunoblotting of HR and NHEJ markers with (B) densitometric analysis of cells treated with FASNi and palmitate. Data plotted as % relative to control of normalized marker expression (marker/vinculin) (n=3-9 over 3 independent experiments, Mean ± SEM). One-way ANOVA with Tukey's test, *p<0.05, **p<0.01, ***p<0.001, ****p<0.0001. (C) Homologous Recombination activity in cells treated with FASNi. Data shown as % relative to control of relative recombination. (n=12 over 3 independent experiments, Mean ± SEM). Unpaired t-test, ****p<0.0001. (D) Luciferase

activity of P53 response element in cells treated with FASNi and palmitate. Data shown as normalized Firefly/Renilla luminescence (n=8 over 2 independent experiments, Mean ± SEM). One-way ANOVA with Tukey's test, ***p<0.001, ****p<0.0001. (E) Representative immunoblotting of phosphorylated P53 (Ser^{15}) (p-P53) in cells treated with FASNi and palmitate. Densitometric analysis (bottom) is also shown, with data plotted as % relative to control of normalized p-P53 to vinculin (n= 3 biological replicates , Mean ± SEM). One-way ANOVA with Tukey's test, *p<0.05.

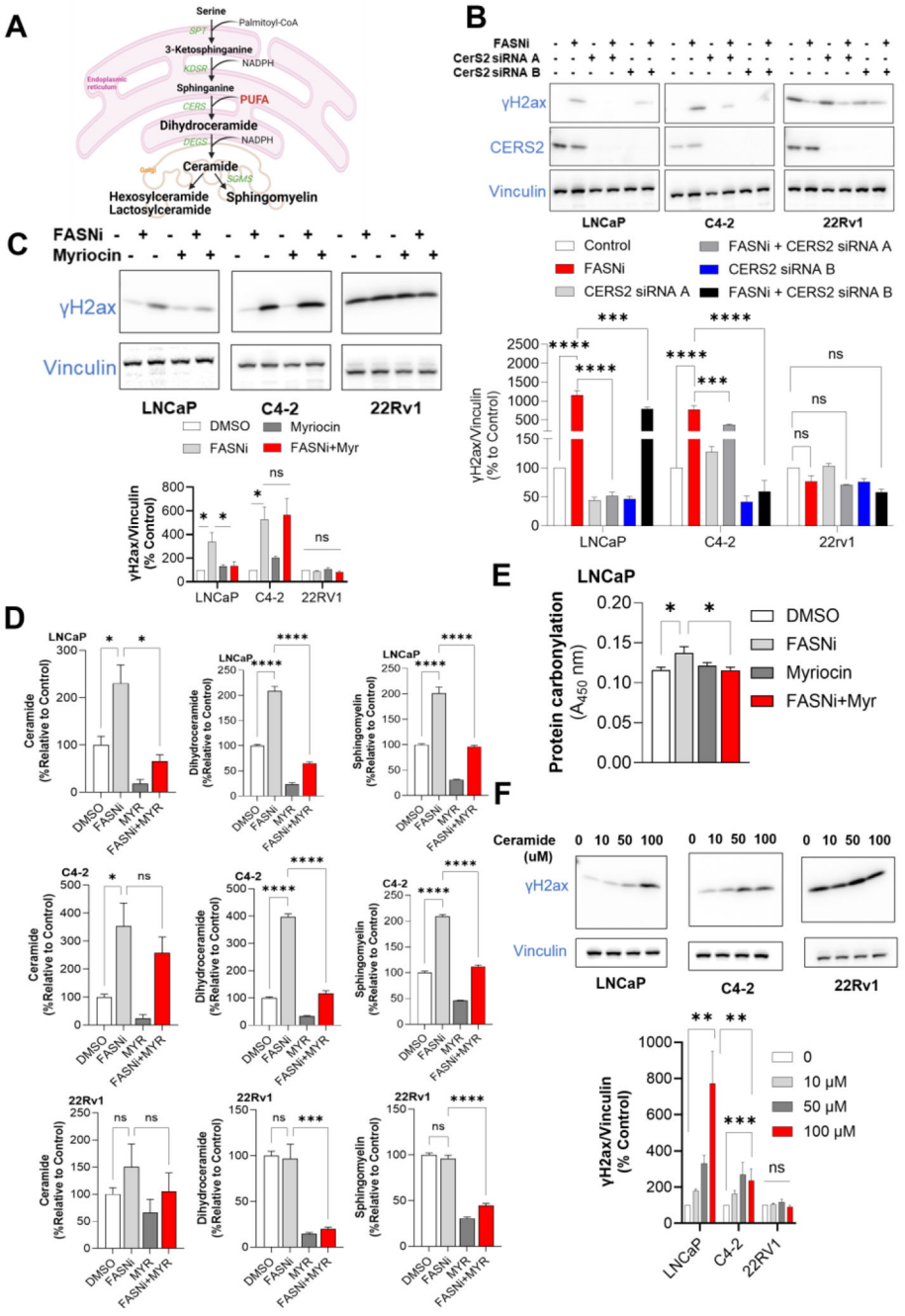

Figure 6. Ceramide synthesis and FASNi-induced DNA damage.

(A) Schematic representation of *de novo* synthesis of ceramide. Serine palmitoyltransferase (SPT), 3-Ketodihydrosphingosine Reductase (KDSR), Ceramide Synthase (CERS), Dihydroceramide Desaturase (DEGS), Sphingomyelin Synthase (SGMS). (B) Representative immunoblotting and densitometric analysis (bottom) of γH2ax following FASNi treatment in cells with CE RS2 knock-down. Data plotted as % relative to control of normalized marker expression (n= 3 biological replicates, Mean ± SEM). One-way ANOVA with Bartlett's test, *p<0.05, ***p<0.001, ****p<0.0001 (C) Representative

immunoblotting and densitometric analysis (bottom) of γH2ax following treatment with FASNi and myriocin. Data shown as % relative to control (n = 3 biological replicates, mean ± SEM). One-way ANOVA with Tukey's test, *p<0.05, ***p<0.001, ****p<0.0001 (D) Modulation of sphingolipid species in cells co-treated with FASNi and myriocin. Total combined sum compositions of ceramide, dihydroceramide and sphingomyelin is shown. Data represented as % relative to control (n = 3, mean ± SEM). One-way ANOVA with Tukey's test, *p<0.05, ***p<0.001, ****p<0.0001. (E) Protein carbonylation abundance in cells treated with FASNi and myriocin. Results are expressed as absorbance at 450 nm (n=12 over 3 independent experiments, mean ± SEM). One-way ANOVA with Tukey's test, *p<0.05, **p<0.01, ***p<0.001. (F) Representative immunoblotting and densitometric analysis (bottom) of γH2ax following treatment with exogenous ceramide (FA 24:1). Data shown as % relative to control (n = 3 biological replicates, mean ± SEM). One-way ANOVA with Dunnett's test, **p<0.01, ***p<0.001

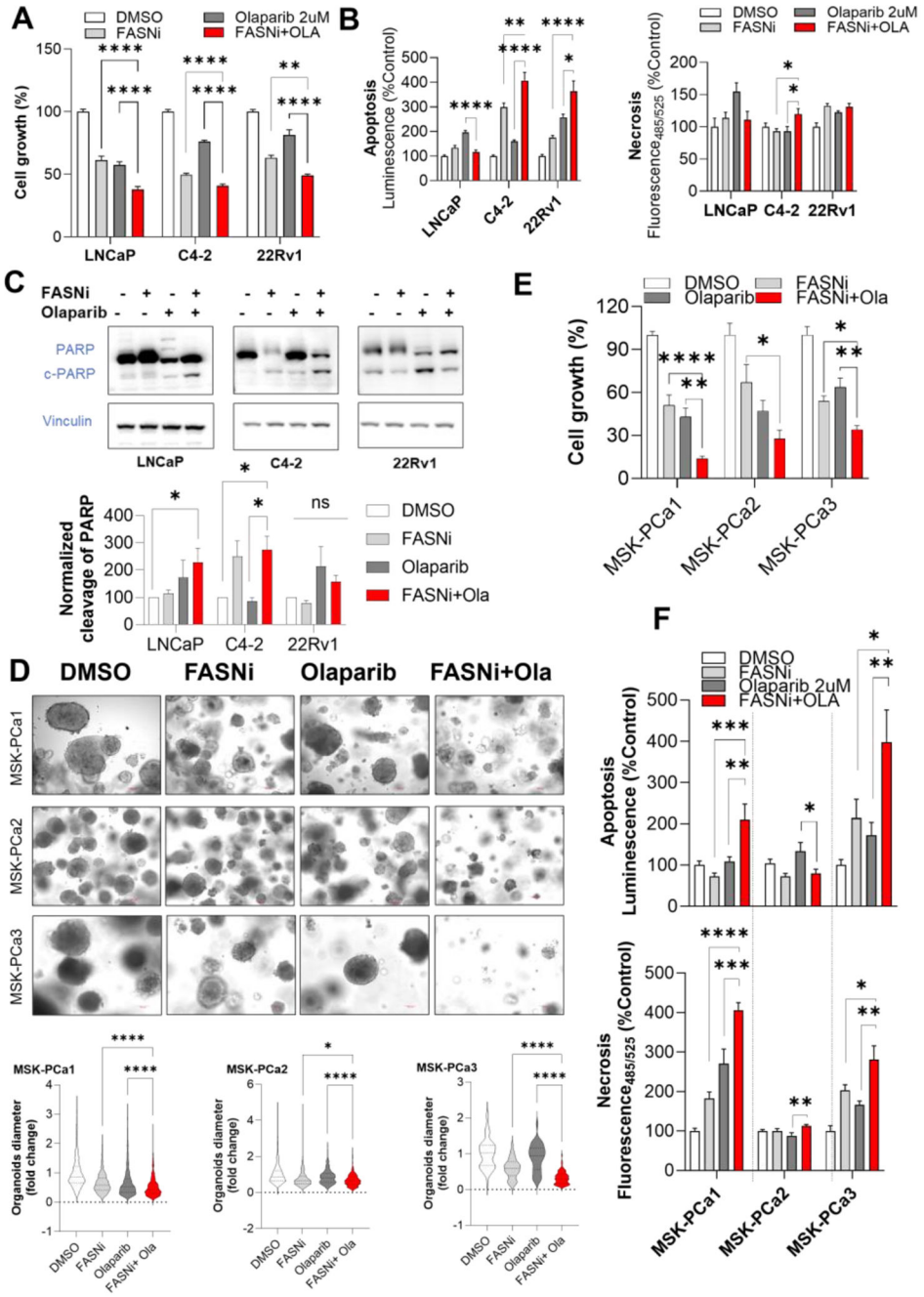

Figure 7. FASN inhibitor in combination with PARP inhibition to target prostate cell growth.

(A) Cell growth assessment after co-treatment with FASNi and Olaparib. Data shown as number of viable cells plotted as % relative to control (n=12-30 replicates over 3 independent experiments, mean ± SEM). One-way ANOVA with Tukey's test, **p<0.01,****p<0.0001. (B) Apoptosis and necrosis abundance in cells following FASNi and Olaparib co-treatment. Data shown as % relative to control (n=6, mean ± SEM). One-way ANOVA with Tukey's test, *p<0.05, **p<0.01, ****p<0.0001. (C) Representative immunoblotting of total and cleaved-PARP and densitometric analysis (bottom) after

co-treatment with FASNi and Olaparib. Results expressed as % relative to control (n = biological replicates, mean ± SEM). One-way ANOVA with Tukey's test, *p<0.05, ***p<0.001, ****p<0.0001 (D) Representative images and statistical analysis (bottom) of MSK-PCa1, MSK-PCa2 and MSK-PCa3 organoids treated with FASNi and Olaparib. Images acquired in brightfield at 10X, scale bar of 100 μm. Diameters of organoids plotted as fold-change to DMSO (n=33-766 organoids, violin plots). One-way ANOVA with Tukey's test, *p<0.05, ****p<0.0001. (E) Organoid cell growth assessment after co-treatment with FASNi and Olaparib. Data shown as number of viable cells plotted as % relative to control (n=6-9, mean ± SEM). One-way ANOVA with Tukey's test, *p<0.05, **p<0.01, ***p<0.001. (F) Apoptosis (RLU) and necrosis (RFU) abundance in organoids treated with FASNi and Olaparib. Data shown as % relative to control (n=14-21, mean ± SEM). One-way ANOVA with Tukey's test, *p<0.05, **p<0.01, ***p<0.001,****p<0.0001.

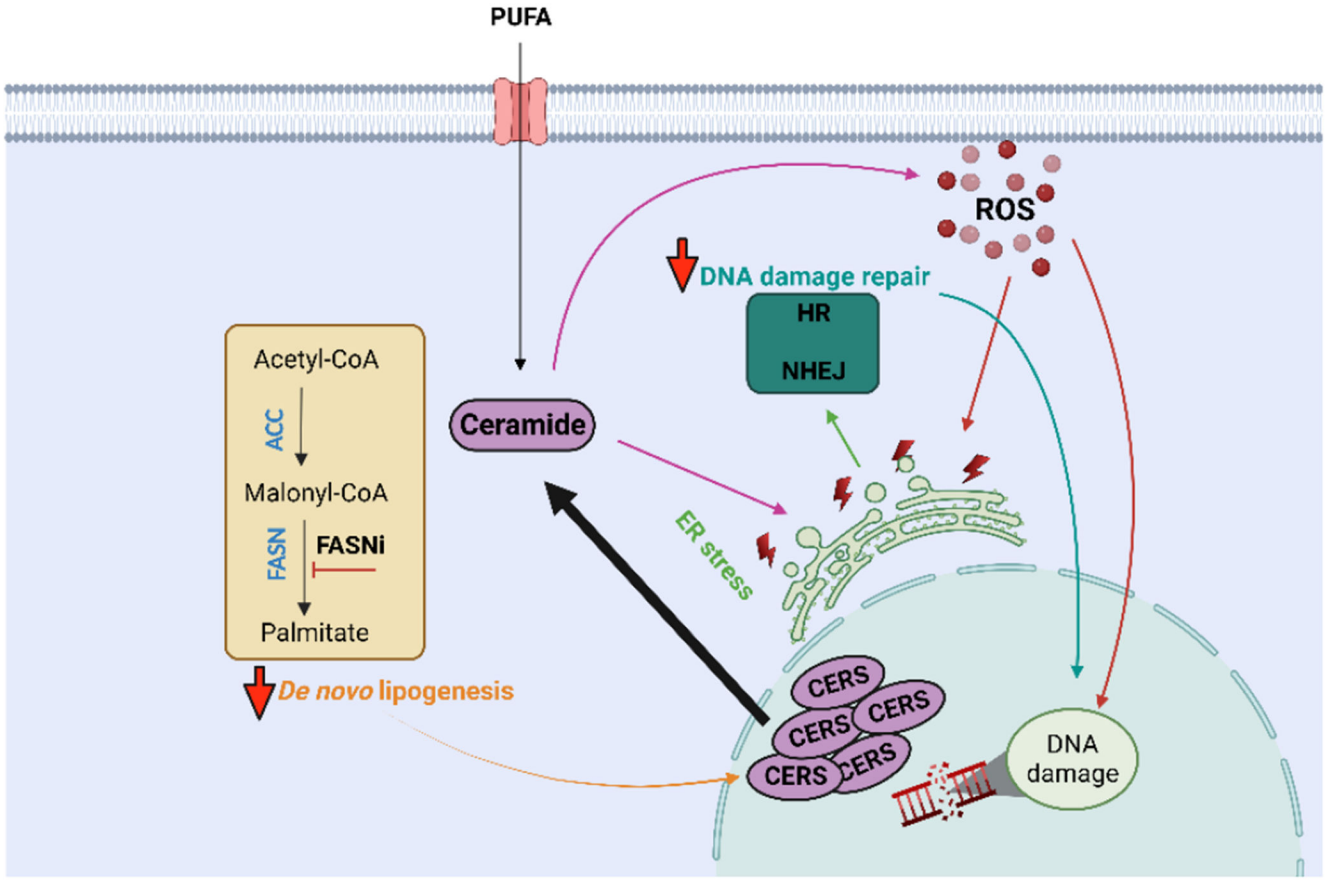

Figure 8. Schematic mechanism of FASN-inhibition-induced DNA damage through rewiring of sphingolipid metabolism and increased oxidative damage.

De novo lipogenesis inhibition by FASN blockade transcriptionally enhances ceramide synthase (CERS), leading to increased abundance of ceramide. Due to polyunsaturated fatty acids (PUFA) utilization by CERS, highly unsaturated and long acyl chains are observed in ceramides and other sphingolipids, inducing oxidative damage through reactive oxygen species (ROS). Reduced protein synthesis is observed, leading to lower expression abundance of enzymes involved in non-homologous end joining (NHEJ) and homologous recombination (HR) pathways. This reduced DNA damage repair capability, allied to increased oxidative damage, culminates in DNA damage in prostate cancer cells (Created with BioRender.com).